Supporting Information for

Metal–organic framework derived tunnel structured MnO as the cathode material for high performance aqueous zinc-ion batteries

Xianwei Li,[a] Qi Liu,[a] Xudong Ma,[a] Pengfei Liu,[b] Donghai Wang,[c] Xiao Yu[d] and Yong Liu*[a]

[a]School of Materials Science and Engineering, State Key Laboratory of Optoelectronic Materials and Technologies, Sun Yat-sen University, Guangzhou 510275, PR. China.

[b]State Key Lab of Solidification Processing, College of Materials Science and Engineering, Northwestern Polytechnical University, Xi'an, Shaanxi, 710072, P. R. China

[c]School of Electronics and Information Technology, Sun Yat-sen University, Guangzhou 510275, P. R. China

[d]College of New Materials and New Energies, Shenzhen Technology University, Shenzhen, 518118，P. R. China

*Corresponding author E-mail: liuyong7@mail.sysu.edu.cn (Y.L.)

Experimental Section

Materials.

N,N-dimethylformamide(DMF), 1,3,5-benzenetricarboxylic acid (1,3,5-H_3BTC), 1,4-benzenedicarboxylic acid (H_2-BDC), $ZnSO_4·7H_2O$, $MnSO_4·H_2O$, $Zn(NO_3)_2·6H_2O$ and $Mn(NO_3)_2·4H_2O$ were purchased from Aladdin Reagent Co. Ltd. (Shanghai, China). The plastic sealing bags were purchased from Deli Group Co., Ltd (Ningbo, China). The graphite paper was purchased from Beihai Carbon Co., Ltd. (Tianjin, China). The coin-type cells (2032) and Glass microfiber filters（420 μm in thickness） were purchased from Guangdong Canrd New Energy Technology. The zinc metal foil (1.0 × 80 × 500 mm) was purchased from Guangzhou Lige Technology Co., Ltd. The graphite crucible (20 mm × 30 mm × 60 mm) was purchased from Baofeng Graphite Products Co. Ltd (Qingdao, China), and cellulose nanofiber (CNF) was purchased from QH Technology Co., Ltd (Guilin, China).

Synthesis of L-MOF-HT and 1D-MOF.

L-MOF-HT and 1D-MOF were synthesized by a solvothermal method. The 1.15 g (4 mmol) of $Mn(NO_3)_2·4H_2O$ and 0.4285 g (2 mmol) of 1,3,5-benzenetricarboxylic acid (1,3,5-H_3BTC) were dissolved in 40 mL of N,N-dimethylformamide(DMF) and 2 mL of deionized water. The mixture was stirred at 25 ℃ for 30 min, then poured into a Teflon-lined stainless steel autoclave (100 mL) and kept at 120 ℃ for 24 h. After cooling to room temperature, the solution was filtered and washed several times with N,N-dimethylformamide (DMF) to obtain a white L-MOF-HT crystalline powder. The resulting L-MOF-HT products were dried overnight at 60 ℃. The effect of reaction time on the evolution of the morphology and crystal structure of the products was also investigated by changing the reaction time from 3 h to 22 h while keeping the other conditions unchanged. The time-dependent products were collected from the Teflon-lined stainless steel autoclave without cooling, then filtered and washed several times with N,N-dimethylformamide(DMF). The 1D-MOF was obtained by keeping the Teflon-lined stainless steel autoclave at 120 ℃ for 5 h with the other conditions unchanged.

Synthesis of t-MnO@C and 1D-MnO@C.

The t-MnO@C and 1D-MnO@C electrodes were obtained by carbonizing L-MOF-HT and 1D-MOF in a tubular furnace at 500 ℃ for 2 h with a heating rate of 1 ℃ min^{-1} under an Ar atmosphere, and then cooled to room temperature with a cooling rate of 2 ℃ min^{-1}, respectively.

Synthesis of MOF-5 and C-MOF-5.

The MOF-5 was synthesized by the previously reported solvothermal method with slight modifications. The 1.74 g (6 mmol) of $Zn(NO_3)_2·6H_2O$ and 0.48 g (3 mmol) of 1,4-benzenedicarboxylic acid (H_2-BDC) were dissolved in 57 g (480 mmol) of N,N-dimethylformamide (DMF). The mixture was stirred at 25 ℃ for 30 min, then the mixture was poured into a Teflon-lined stainless steel autoclave (100 mL) and kept at 120 ℃ for 21 h. After cooling to room temperature, the solution was filtered and washed several times with N,N-dimethylformamide (DMF) to give a white crystalline powder. The resulting products were dried at 60 ℃ overnight. The MOF-5 was poured into a graphite crucible (20 mm × 30 mm × 60 mm) and then carbonized in a tube furnace at

800 ℃ for 2 h with a heating rate of 1 ℃ min^{-1} under an Ar atmosphere, and then cooled to room temperature with a cooling rate of 2 ℃ min^{-1} to obtain C-MOF-5.

Material characterizations.

The morphologies of samples were observed by a thermal field emission scanning electron microscopy (Quanta 400, FEI Company; Gemini500, Bruker). Transmission electron microscopy (TEM), high-resolution transmission electron microscopy (HRTEM), and selected area electron diffraction (SAED) patterns were conducted by a transmission electron microscope (Fei TECNAI G2 F30) with an acceleration voltage of 300 kV. The ex-situ TEM analysis was conducted by combining the transmission electron microscope (Fei TECNAI G2 F30) with the direct-detection electron-counting camera (Gatan K2 Summit). The structure of materials was characterized using an X-ray diffraction (D8 Advance, Bruker) with Cu Kα radiation (λ = 0.15405 nm). Raman spectra were obtained on a microscopic confocal Raman spectrometer (Horiba Jobin Yvon XploRa) with 532 nm incident laser excitation. X-ray photoelectron spectra (XPS) were measured on an X-ray photoelectron spectroscopy (ESCALab MKII) with an excitation source of Mg Kα radiation (1,253.6 eV). The N_2 adsorption–desorption isotherms were carried out at 77 K by using a gas sorption analyzer (NOVA1200 instrument, Quantachrome Corporation). Thermogravimetry (TG) curves were obtained on a thermogravimetric analyzer (TGA/DSC 3+, Mettler) at temperatures from the room temperature to 800 °C in air at a heating rate of 10 °C min^{-1}.

Single-crystal x-ray diffraction (SCXRD).

The SCXRD data of all samples were collected by an Agilent SuperNova diffractometer with a 4-circle kappa goniometer, a micro-focus high-brilliance source with Cu Kα radiation (λ = 0.15418 nm) and an Eos CCD detector at an ambient temperature of 150 k. The data were treated by the CrysAlisPro software, and the absorption correction by using spherical harmonics. Solution and refinement of the crystal structure were performed by using the SHELX algorithms in Olex2 software. Further details of the structure investigations of 1D-MOF and L-MOF-HT can be obtained from The Cambridge Crystallographic Data Centre via www.ccdc.cam.ac.uk/data_request/cif, on quoting the depository number CCDC 2143646 and 2143647, respectively.

Electrochemical measurements.

The cathode slurry was prepared by mixing the active materials (t-MnO@C and 1D-MnO@C), acetylene black and Cellulose nanofiber (CNF) with a mass ratio of 8:1:1 in deionized water. The cathodes were prepared by coating the slurry on graphite paper with a size of 1×1 cm^2 and thickness of 130 μm, and then dried at 100 ℃ overnight in a vacuum oven. The mass loading of active materials was controlled at 1.3-1.5 mg cm^{-2}, and its area and thickness were controlled at 1×1 cm^2 and approximately 10 μm, respectively. The anode (C-MOF-5@Zn) was prepared by coating the slurry containing C-MOF-5 (80%) and cellulose nanofiber (CNF) (20%) on pure Zn foil, and the film thickness was controlled at 15-20 μm. The pure Zn foil has a size of 1×1 cm^2 and thickness of 100 μm. C-MOF-5@Zn||t-MnO@C and C-MOF-5@Zn||1D-MnO@C soft-package cells were assembled by using the C-MOF-5@Zn as the anode, glass microfiber filter (420 μm thick, Whatman GF/F) as the separator, t-MnO@C and 1D-MnO@C as the cathode, and 2 M $ZnSO_4$ + 0.1 M $MnSO_4$ aqueous solution as the electrolyte, which were then encapsulated in the plastic sealing bags by means of heat

sealing. The amount of electrolyte used is approximately 0.4 mL in each cell. For comparison, Zn||t-MnO@C soft-package cells were assembled by using bare Zn foil as anode and t-MnO@C as cathode; and for calculation of discharge capacity of t-MnO@C, C-MOF-5@Zn||graphite paper also assembled by using C-MOF-5@Zn as anode and graphite paper as the counter electrode while keeping other conditions unchanged. The symmetric C-MOF-5@Zn||C-MOF-5@Zn (or Zn||Zn) batteries were assembled in CR2032-type coin cells by sandwiching glass a microfiber filter separator between two C-MOF-5@Zn (or Zn||Zn) electrodes and filled with electrolyte of 2 M $ZnSO_4$ and 0.1 M $MnSO_4$ aqueous solution (pH = 4.7). Galvanostatic discharge-charge curves were measured using a multichannel battery test system (BT2043, Arbin Instruments). The Cyclic voltammograms (CV) experiments were carried out at scan rate of 0.1, 0.2, 0.4, 0.8, 1, 2 and 3 mV s^{-1} by using an electrochemical working station (Autolab, PG STAT302N, Metrohm-Autolab B.V.). All electrochemical performances were tested in the potential range of 0.8~1.9 V at 25 °C. The corrosion-resistant capability was analyzed based on the linear polarization method in a three-electrode cell, in which C-MOF-5@Zn or bare zinc foil was applied as the working electrode, a Pt plate as the counter electrode, Ag-AgCl electrode as the reference electrode and 2 M $ZnSO_4$ solution as electrolyte.

Ex-situ analysis.

For ex-situ XRD and XPS measurements, the cells at various discharge/charge states were disassembled to obtain the ex-situ cathodes. Then, these ex-situ electrodes were washed with distilled water several times for removing the adhered white fibers from it. After that, they were dried at 80 °C for 24 h in vacuum before measurements. For the ex-situ TEM measurement, the ex-situ electrodes at fully charge and discharge states of 1st cycle were obtained by the same procedure as above, and the obtained cathode materials were dispersed in alcohol by ultrasound. Then, the dispersed of cathode materials were dripped on the copper mesh by capillary burette to prepare the ex-situ TEM samples.

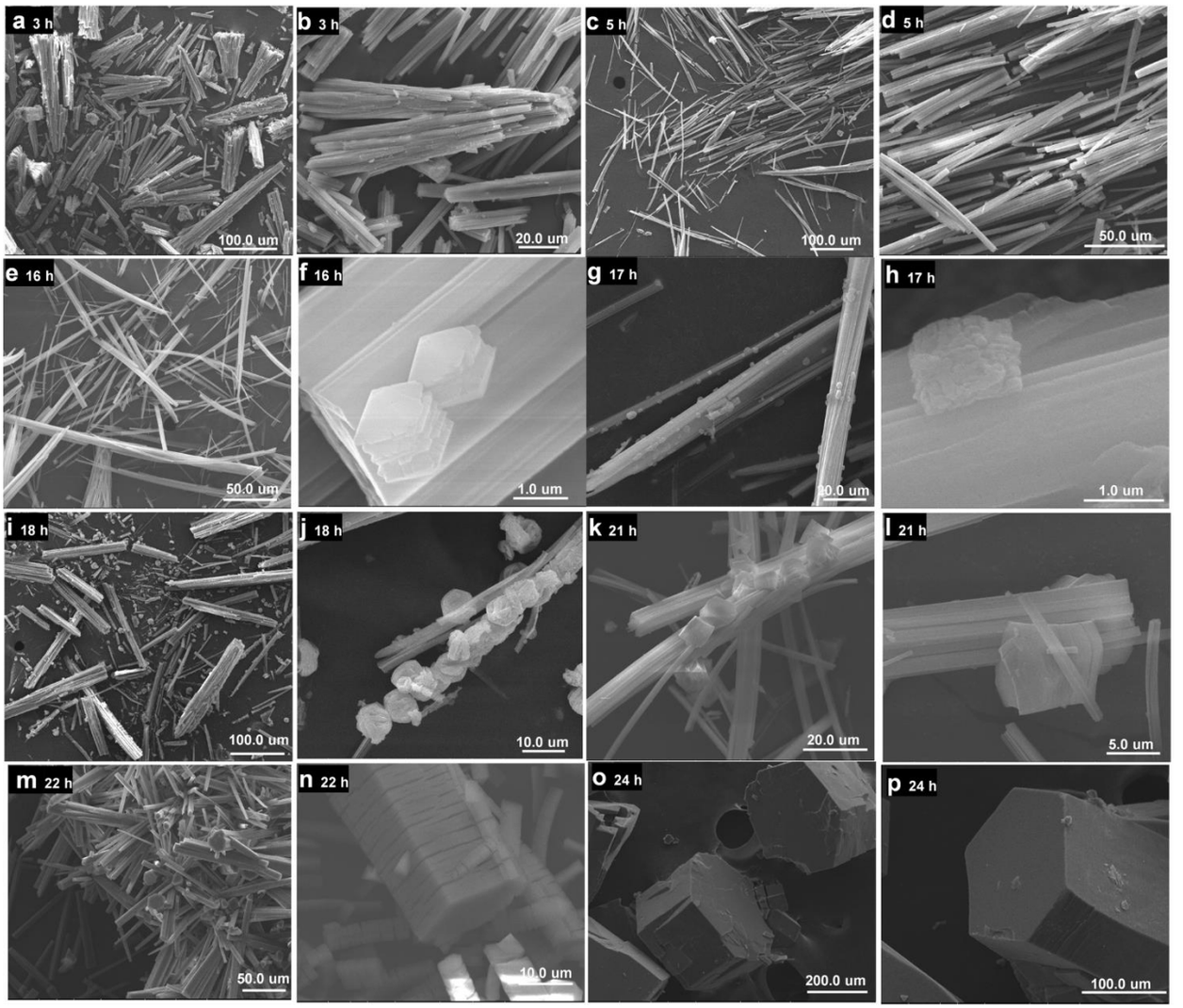

Fig. S1 SEM images of the growth process of L-MOF-HT through a MOF-on-MOF epitaxial growth and dissolution-recrystallization reaction. Samples were collected after the hydrothermal treatment at 120 °C for (a, b) 3 h, (c, d) 5 h, (e, f) 16 h, (g, h) 17 h, (i, j) 18 h, (k, l) 21 h, (m, n) 22 h, and (o,p) 24 h, respectively.

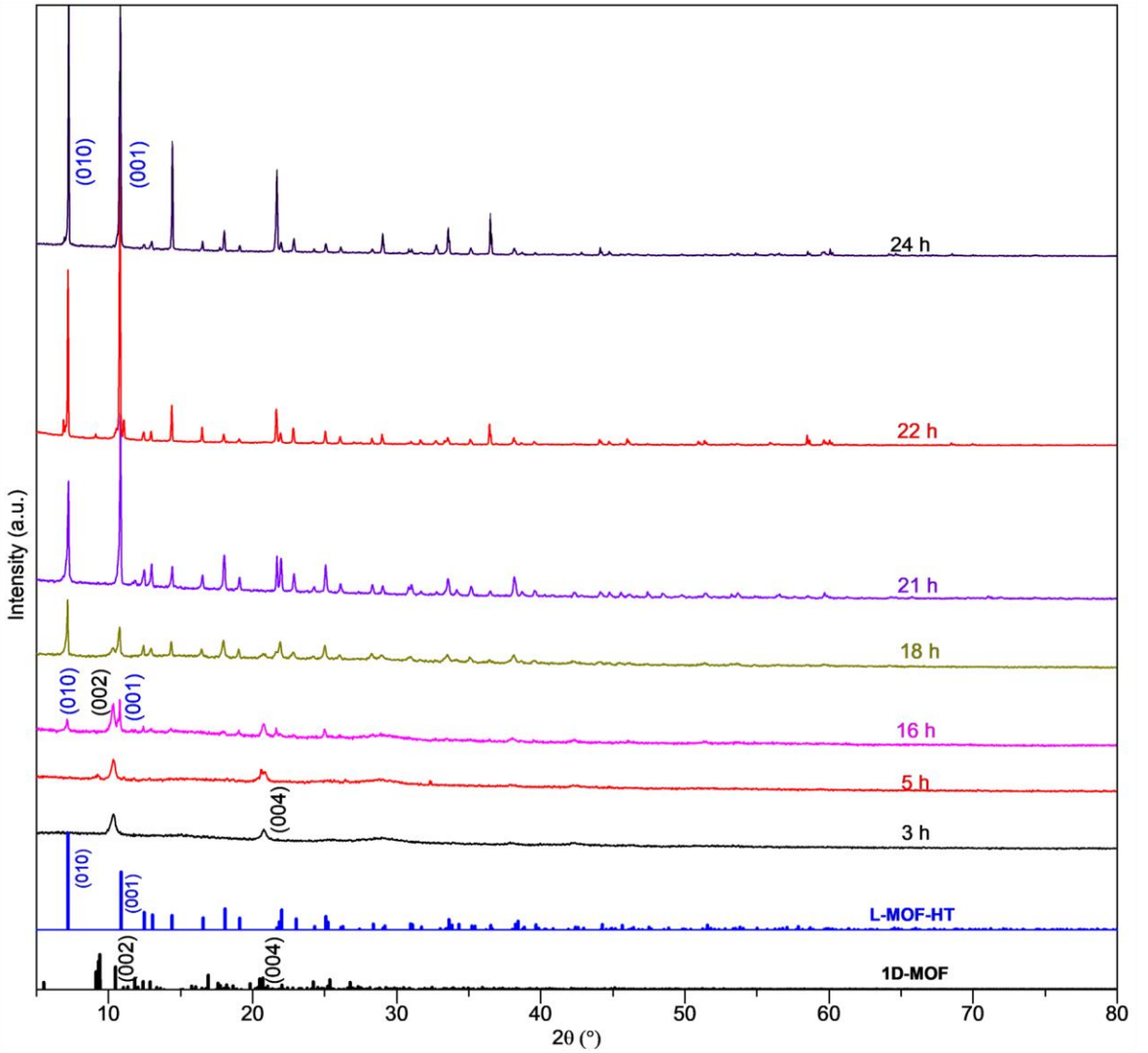

Fig. S2 Time-dependent PXRD patterns for the transformation of 1D-MOF to L-MOF-HT. The simulated single-crystal XRD patterns of L-MOF-HT and 1D-MOF are also shown.

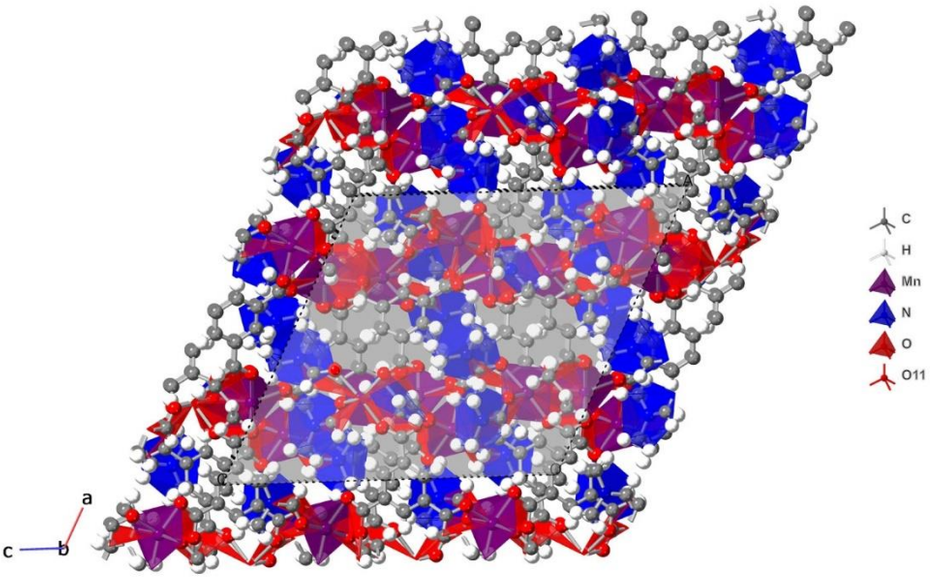

Fig. S3 Single-crystal structure of 1D-MOF viewed along the b-axis. C atoms, grey; N atoms, blue. H atoms, white. O atoms, red. Mn atoms, purple.

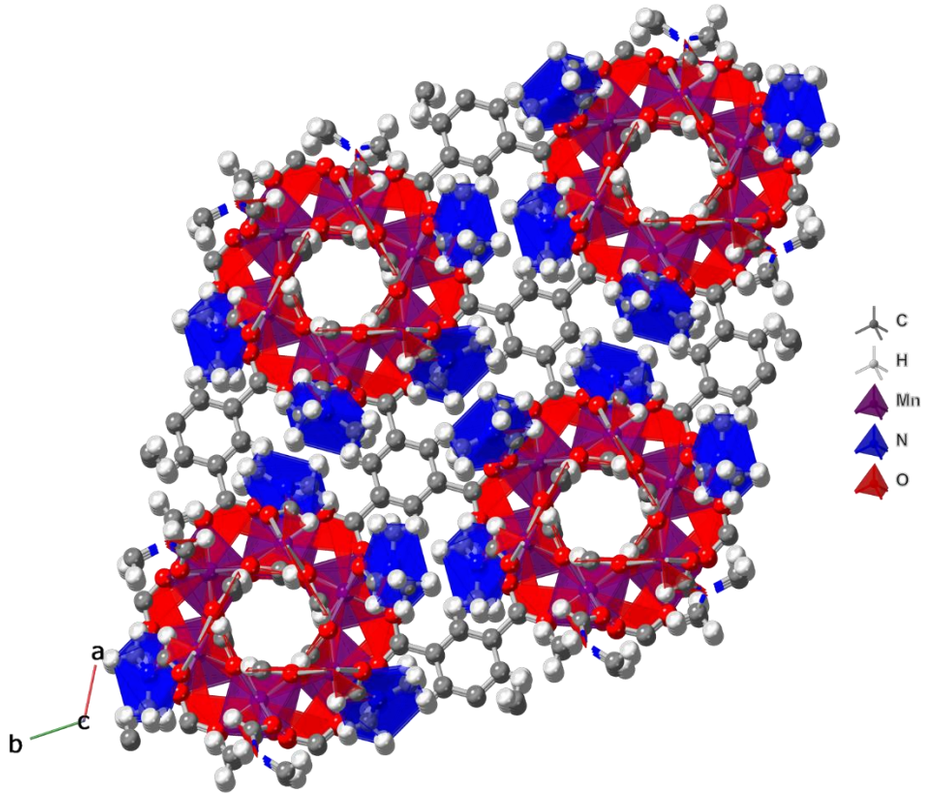

Fig. S4 Single-crystal structure of L-MOF-HT viewed along the c-axis. C atoms, grey; N atoms, blue. H atoms, white. O atoms, red. Mn atoms, purple.

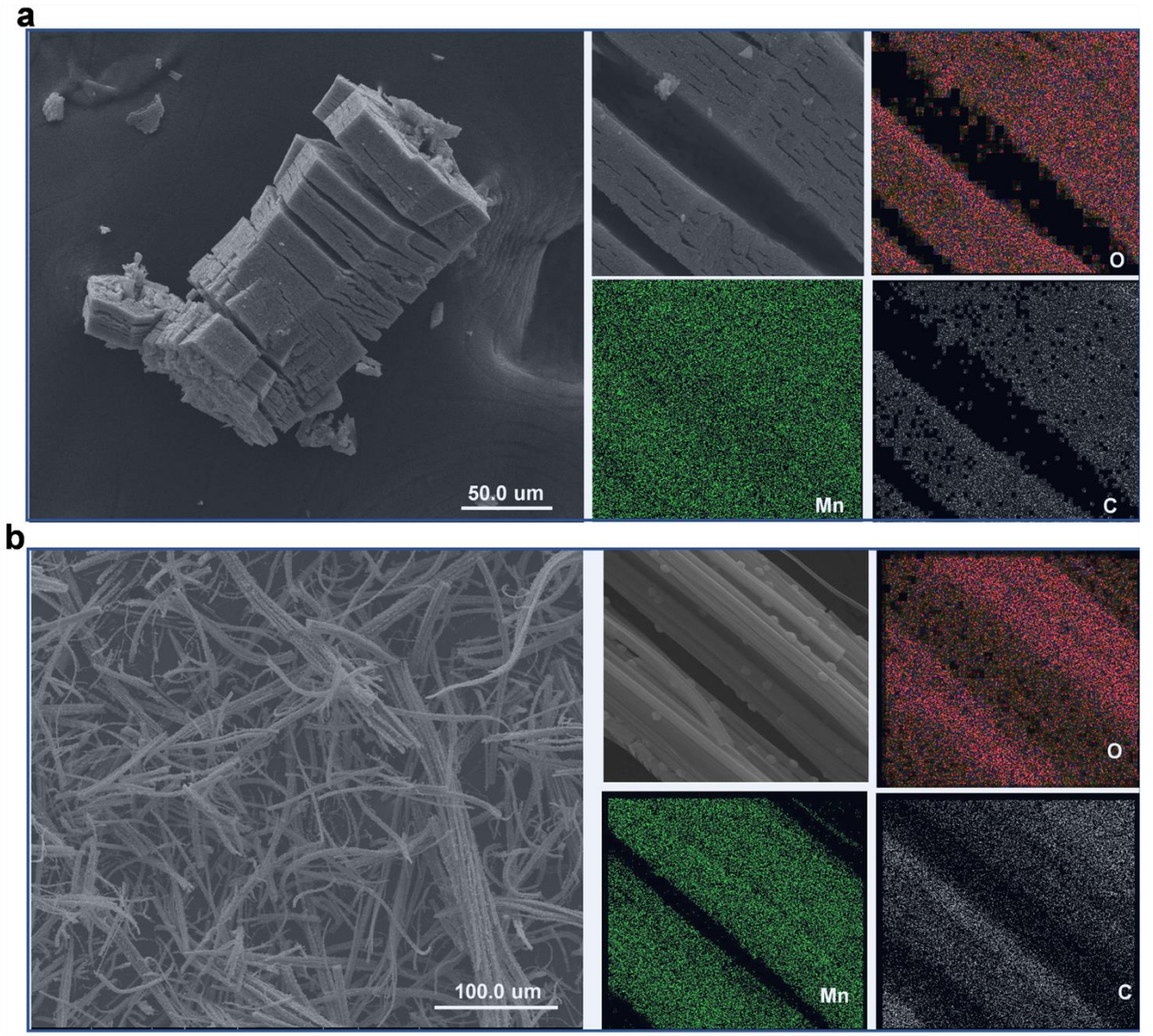

Fig. S5 SEM and EDX images of (a) t-MnO@C and (b) 1D-MnO@C samples.

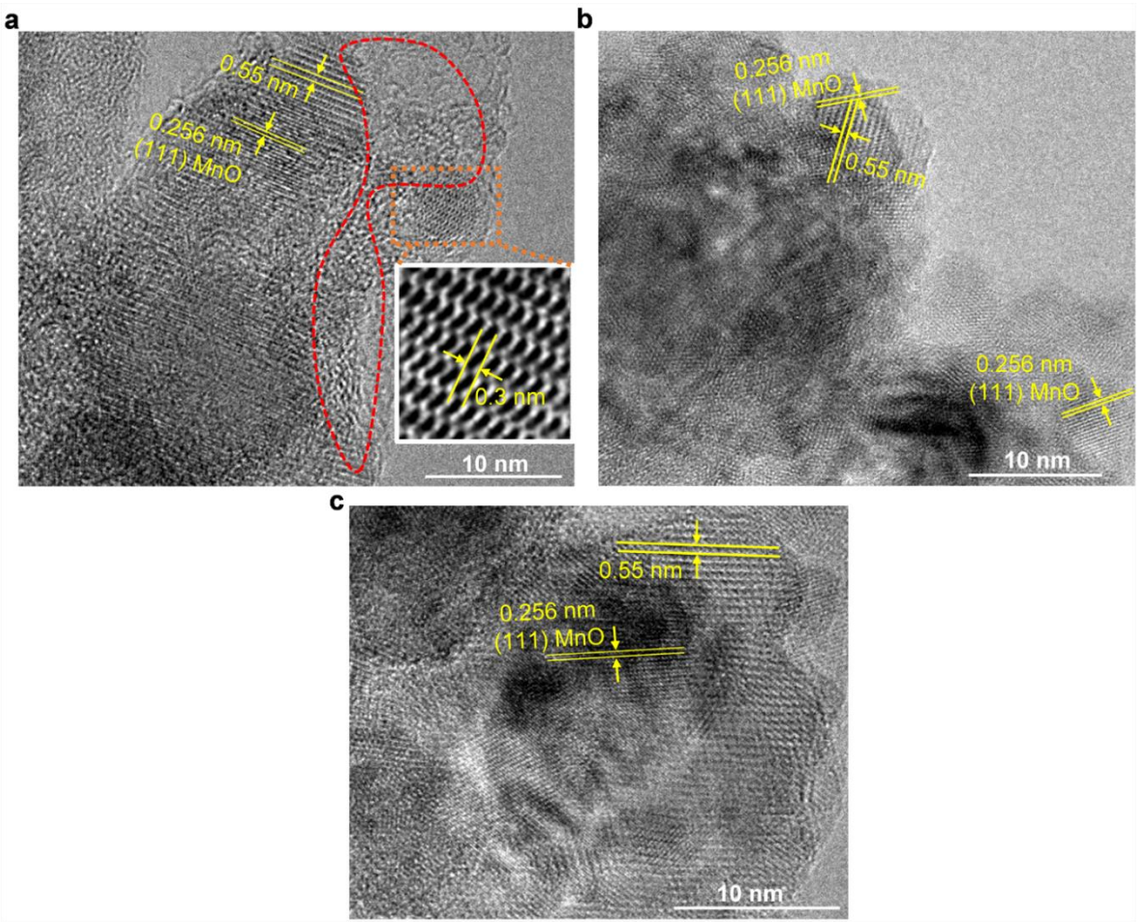

Fig. S6 (a-c) HRTEM images of the t-MnO@C. The d-spacing of 0.55 nm in t-MnO@C is retained and derived from the hexagonal tunnels of the original L-MOF-HT (d～0.6009 nm).

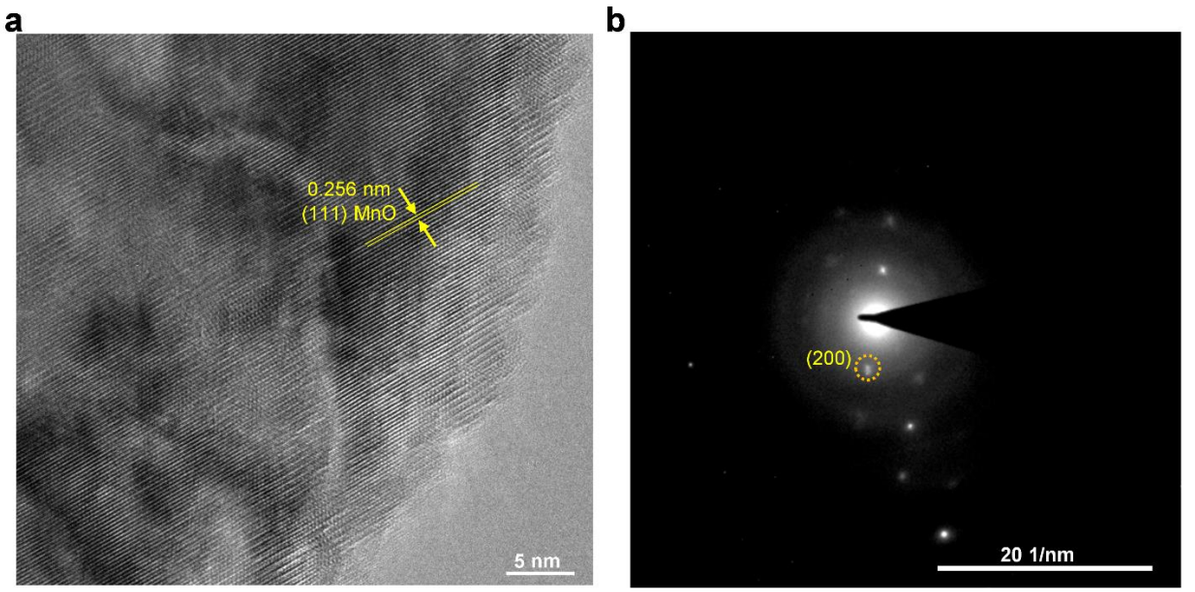

Fig. S7 (a) HRTEM image and (b) SAED pattern of the 1D-MnO@C, which only contain MnO phase without tunnels.

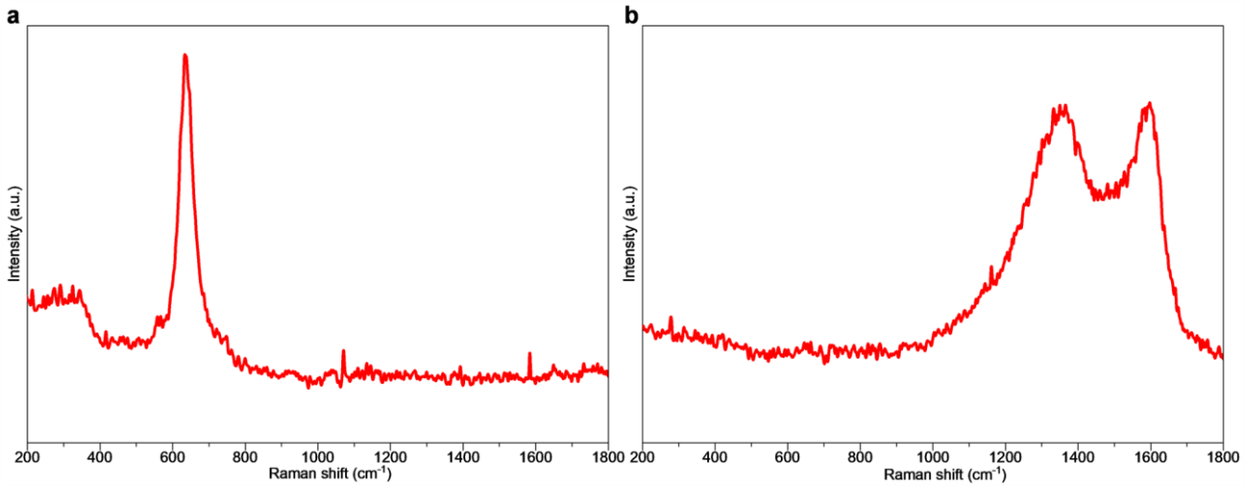

Fig. S8 Raman spectra of (a) the t-MnO@C without treatment and (b) the t-MnO@C after removing Mn^{2+} ions by soaking it in 1 M H_2SO_4 solution for 12 h.

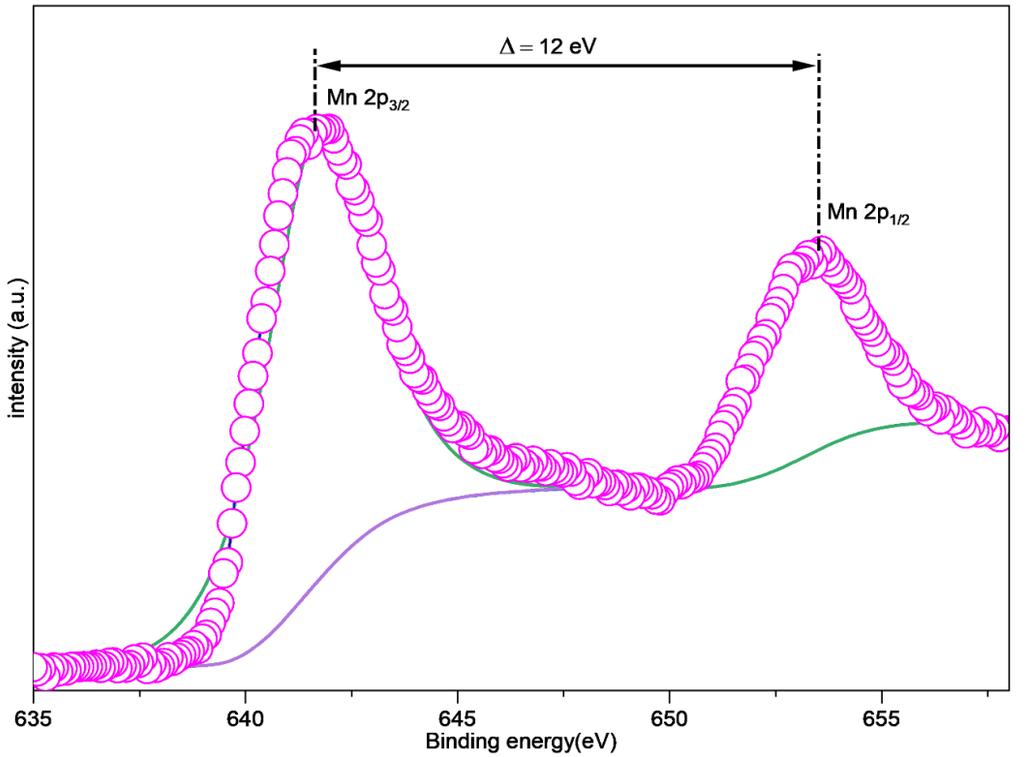

Fig. S9 High-resolution Mn 2p XPS spectrum of t-MnO@C.

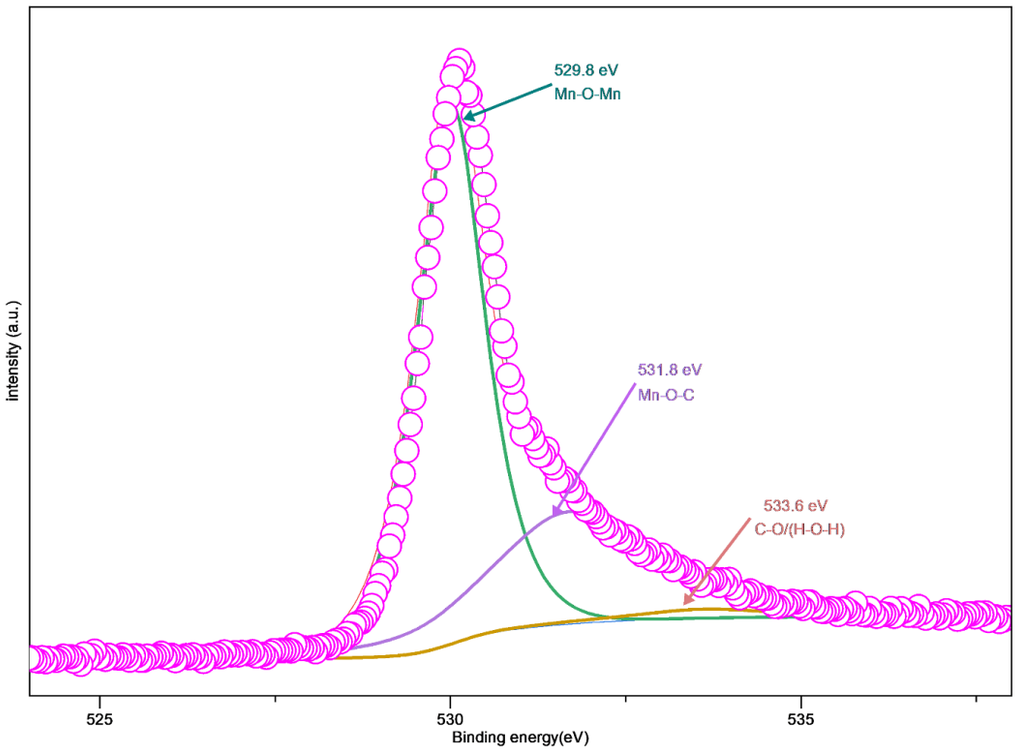

Fig. S10 High-resolution O1s XPS spectrum of the t-MnO@C.

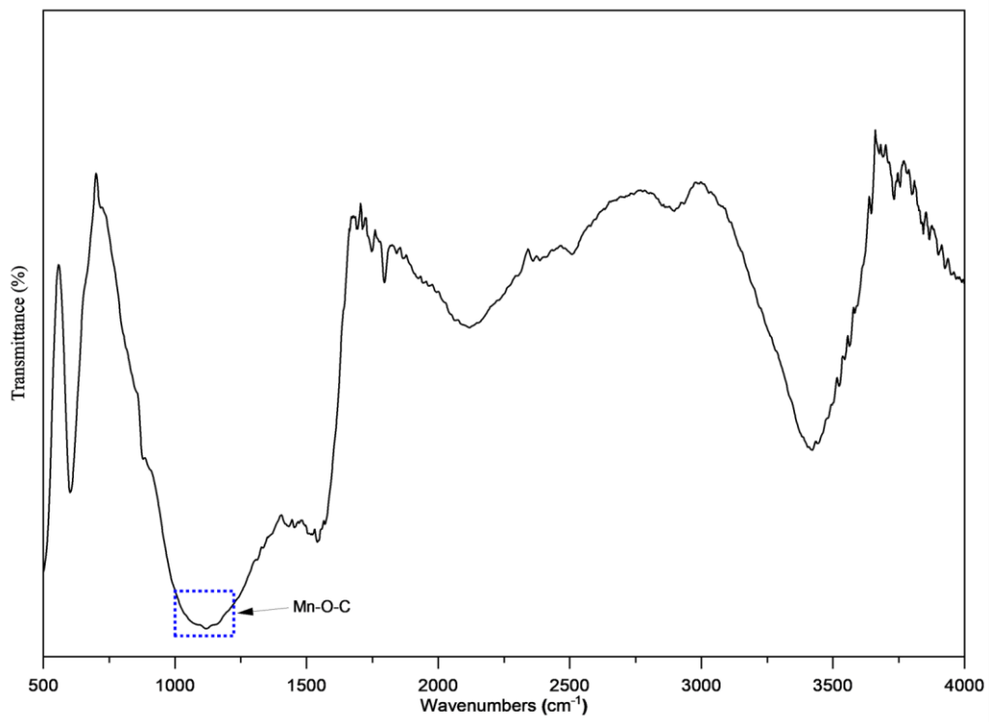

Fig. S11 FTIR spectrum of t-MnO@C.

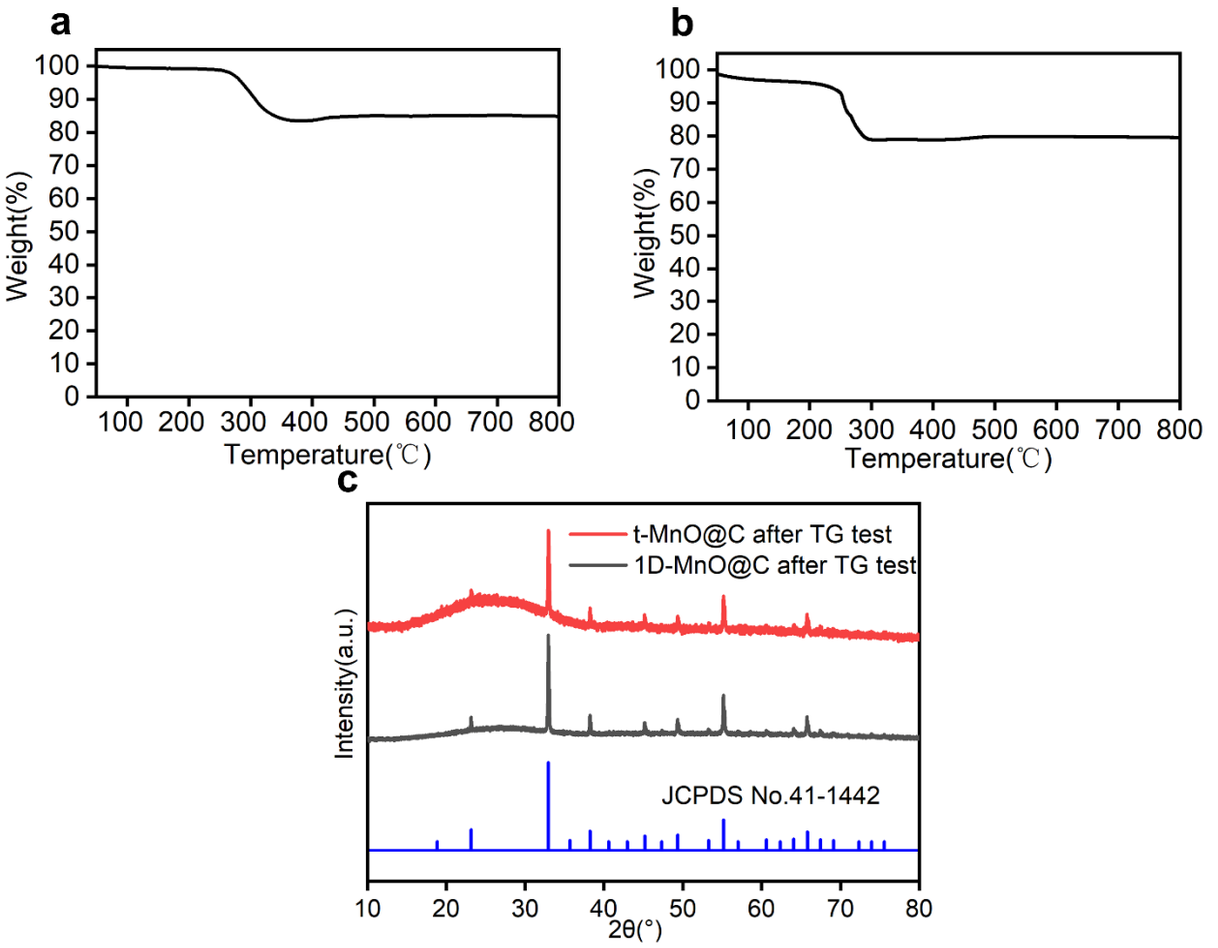

Fig. S12 TG profiles of (a) the t-MnO@C and (b) 1D-MnO@C tested under air flow; (c) XRD pattern of residues of t-MnO@C and 1D-MnO@C after TGA test, indicating the formation of Mn_2O_3 (JCPDS No.41-1442) at 800 ℃.

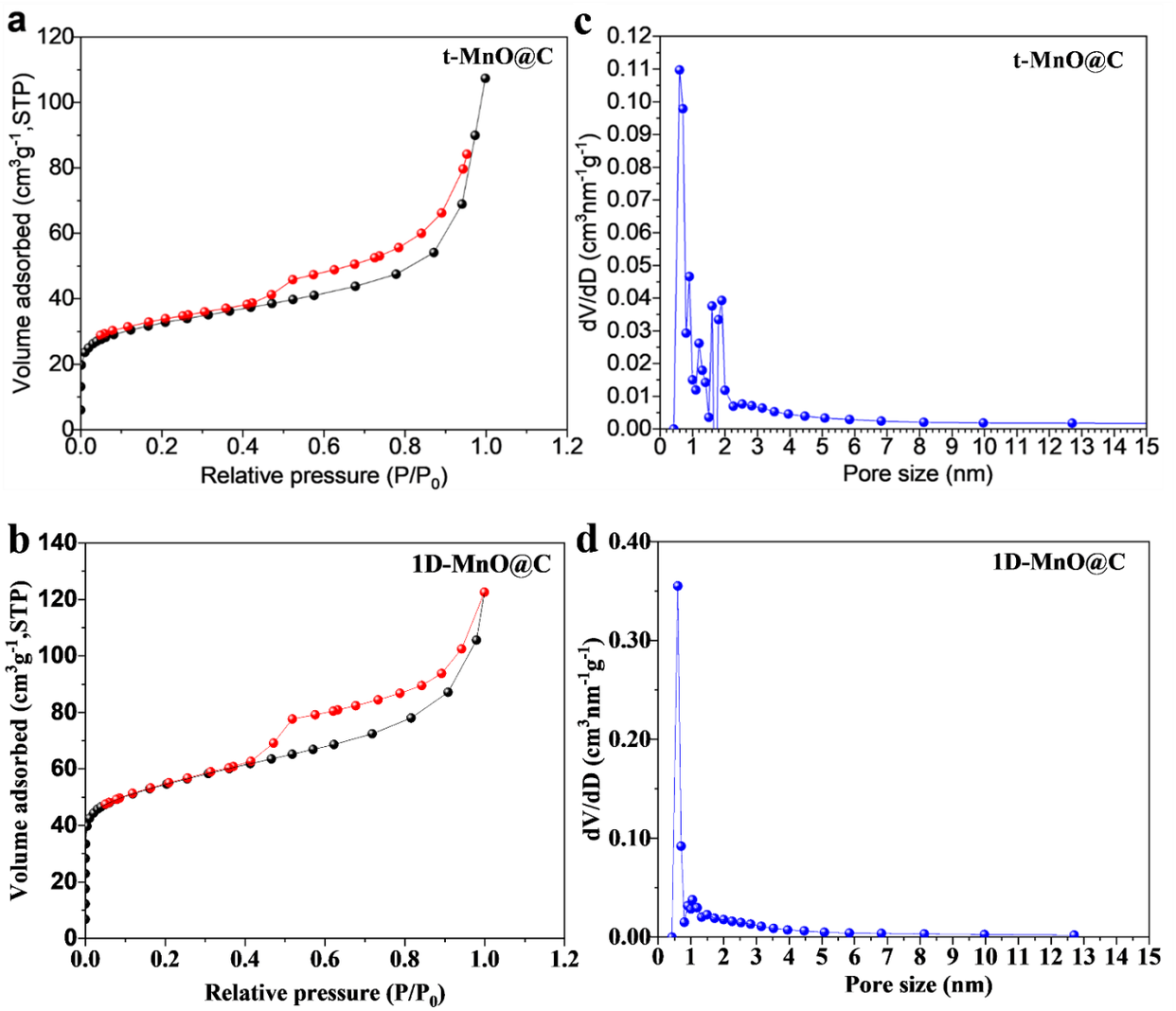

Fig. S13 N_2 adsorption/desorption isotherms of (a) the t-MnO@C and (b) the 1D-MnO@C samples; pore size distribution of (c) the t-MnO@C and (d) the 1D-MnO@C samples.

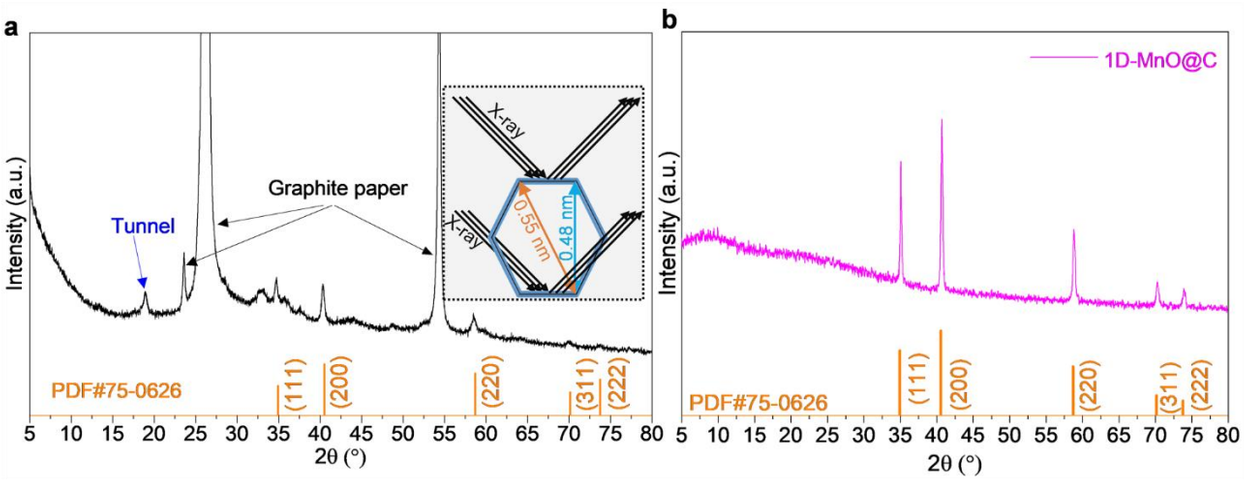

Fig. S14 PXRD patterns of t-MnO@C (a) and 1D -MnO@C (b) electrodes.

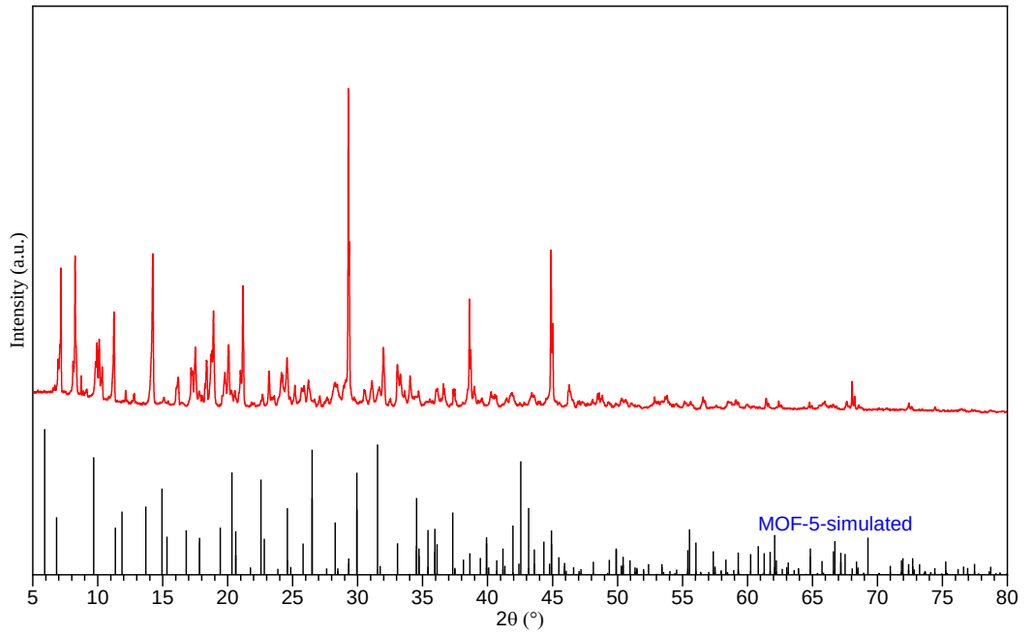

Fig. S15 PXRD pattern and simulated PXRD pattern of MOF-5.

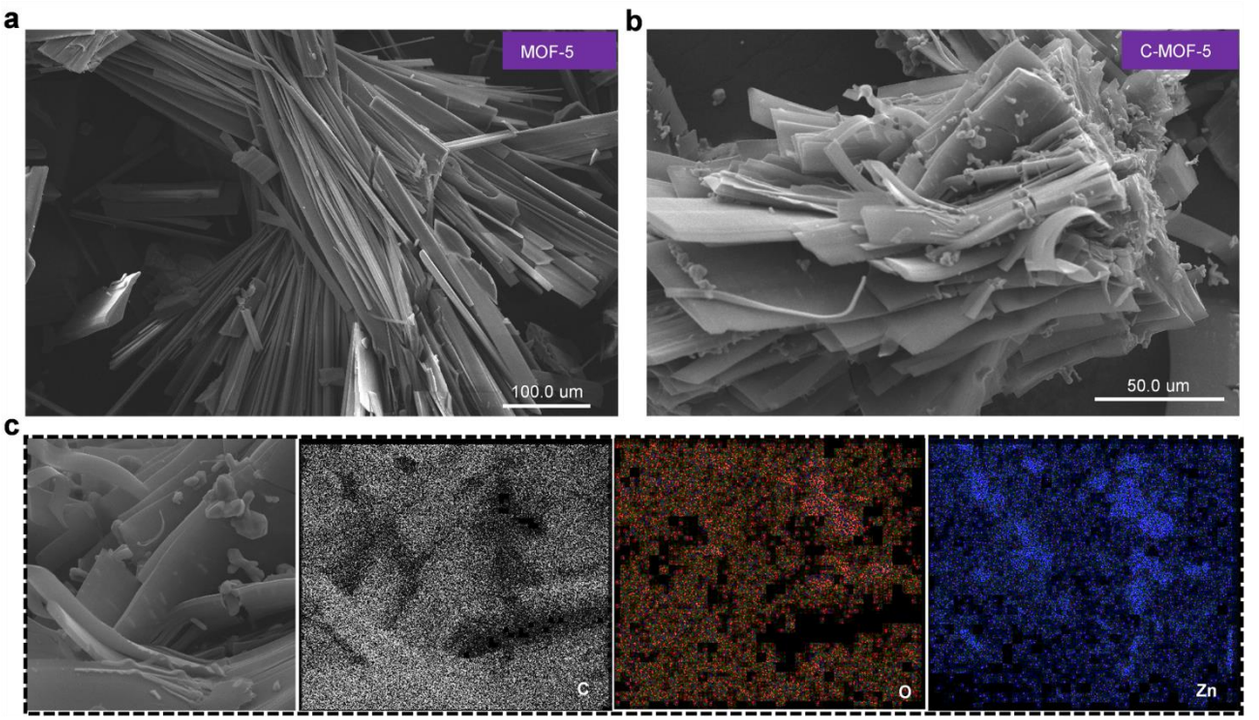

Fig. S16 SEM images of (a) MOF-5 and (b) C-MOF-5; (c) SEM image and corresponding elemental mapping images of the C-MOF-5.

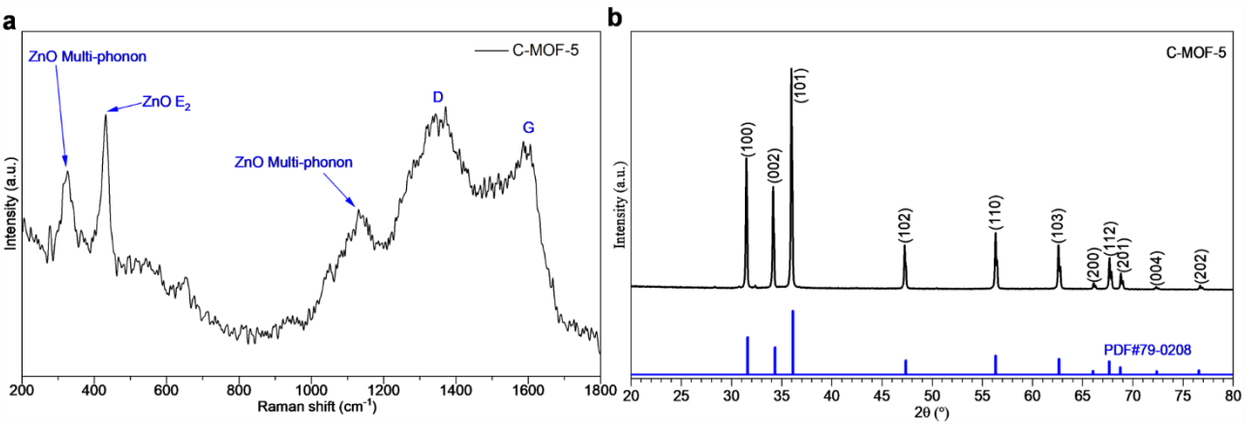

Fig. S17 (a) Raman spectrum of C-MOF-5, (b) PXRD patterns of ZnO contained in C-MOF-5.

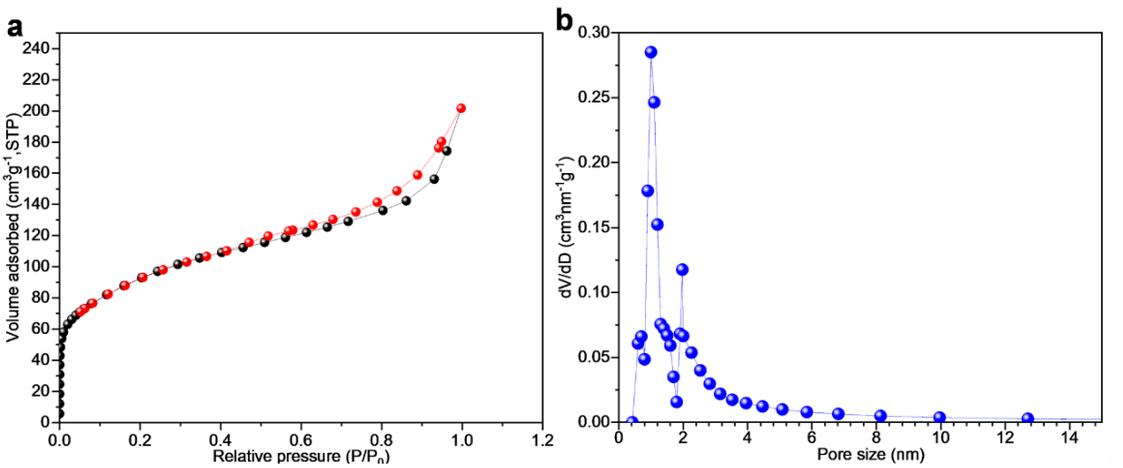

Fig. S18 (a) N_2 adsorption/desorption isotherms and (b) pore size distribution of the C-MOF-5.

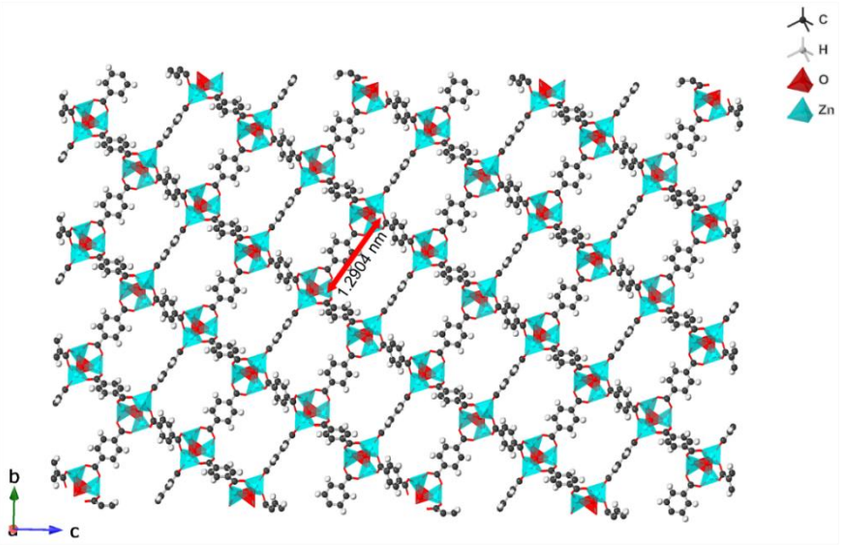

Fig. S19 Single-crystal structure of MOF-5 viewed along a-axis. C atoms, grey. Zn atoms, green. H atoms, white. O atoms, red.

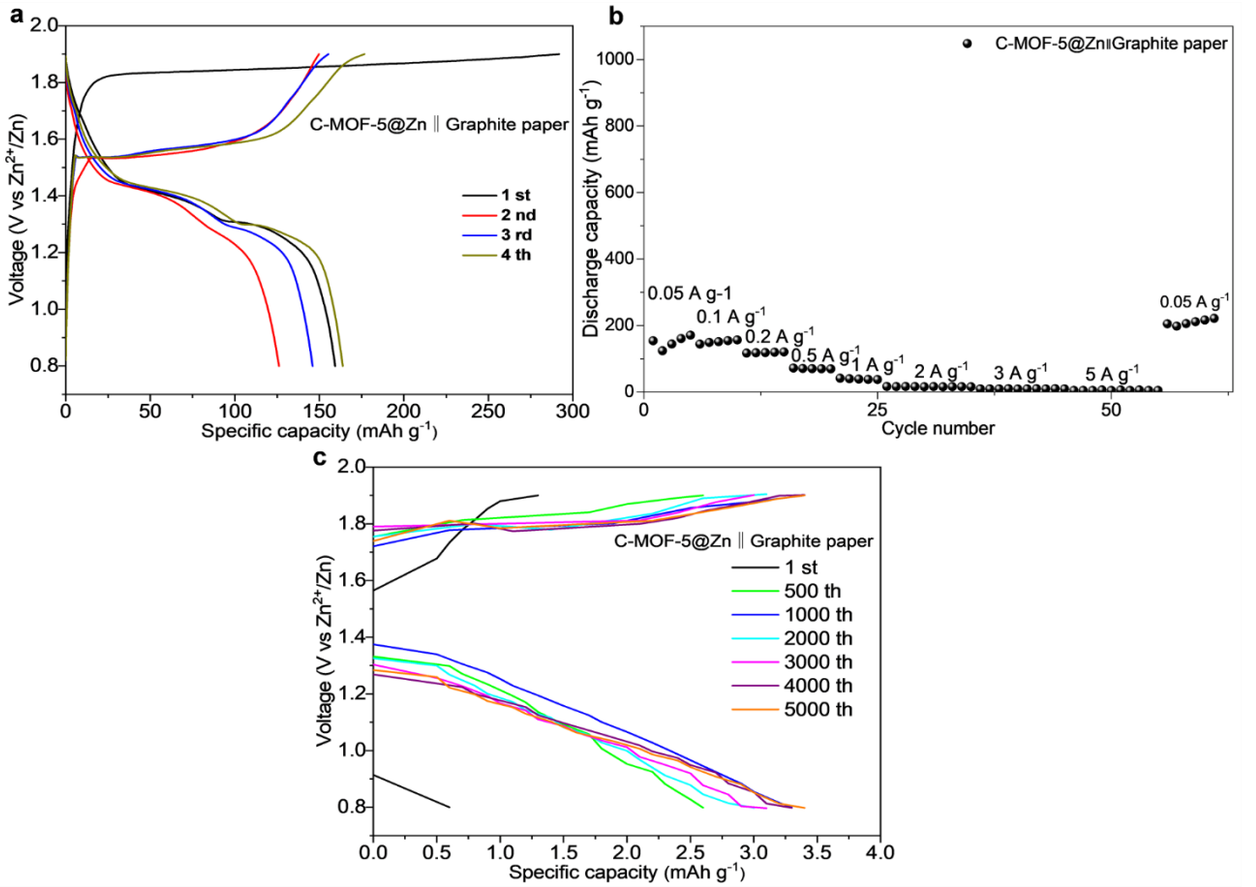

Fig. S20 (a) Galvanostatic charge/discharge profiles at a current density of 0.05 A g^{-1}, (b) rate performance (discharge capacity) and (c) galvanostatic charge/discharge profiles at a current density of 5 A g^{-1} of graphite paper in the C-MOF-5@Zn||graphite paper cell.

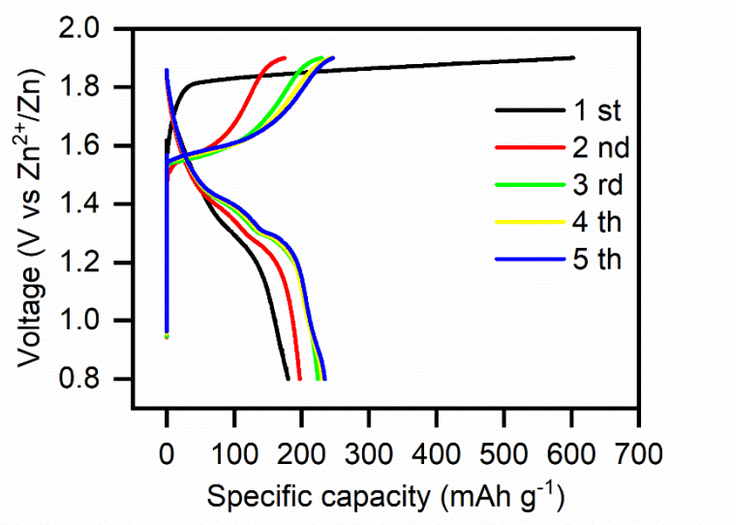

Fig. S21 Galvanostatic charge/discharge profiles of carbon framework in the C-MOF-5@Zn‖carbon framework cell tested at a current density of 0.05 A g^{-1}.

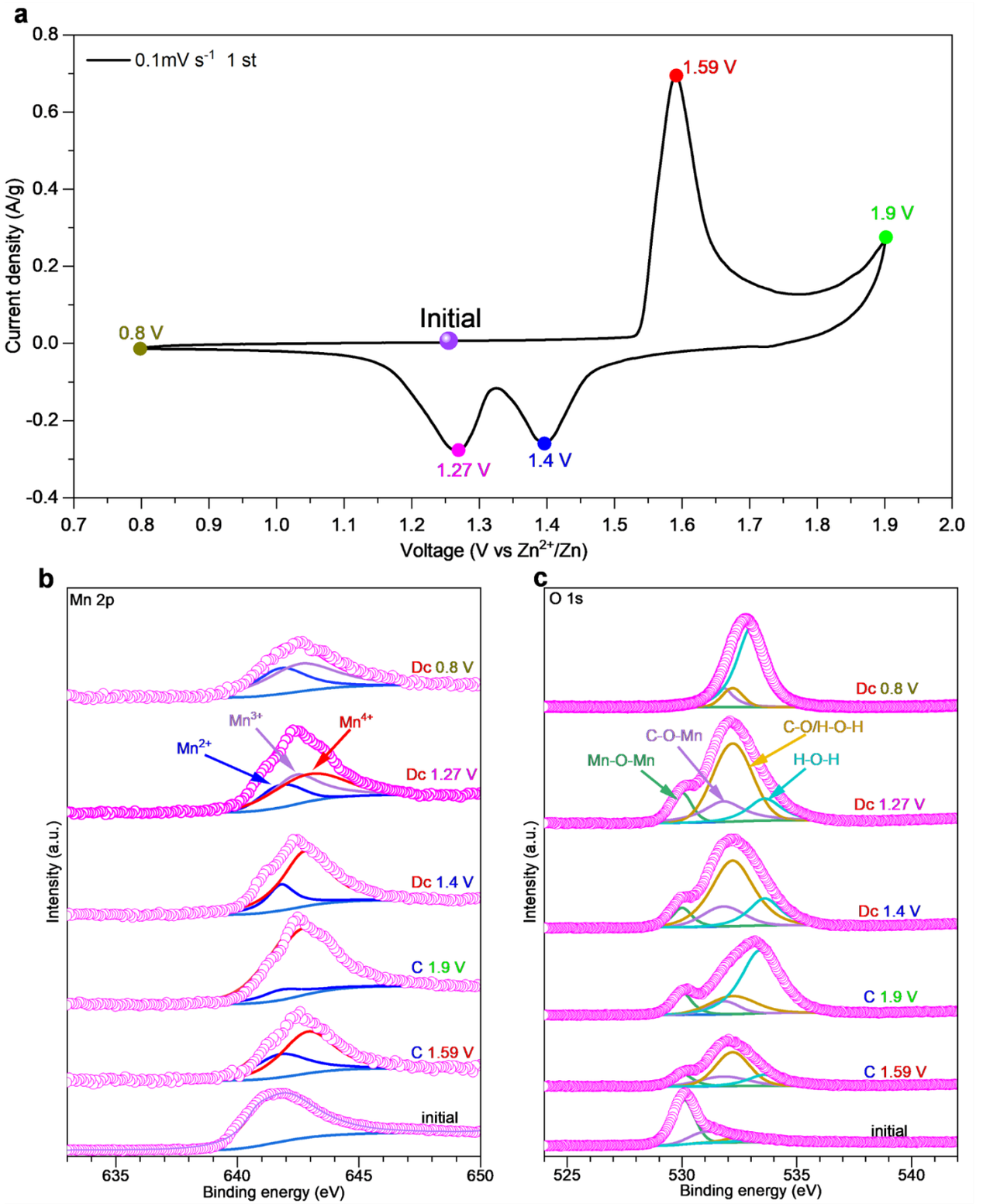

Fig. S22 Ex-situ XPS spectra of Mn 2p (b), and O 1s (c) at different states during the first CV scan at a scan rate of 0.1 mV s^{-1} (a) for the t-MnO@C electrode in the C-MOF-5@Zn||t-MnO@C soft-package cells. In Fig. S22b and 22c, "C" represents charge state; "Dc" represents discharge state.

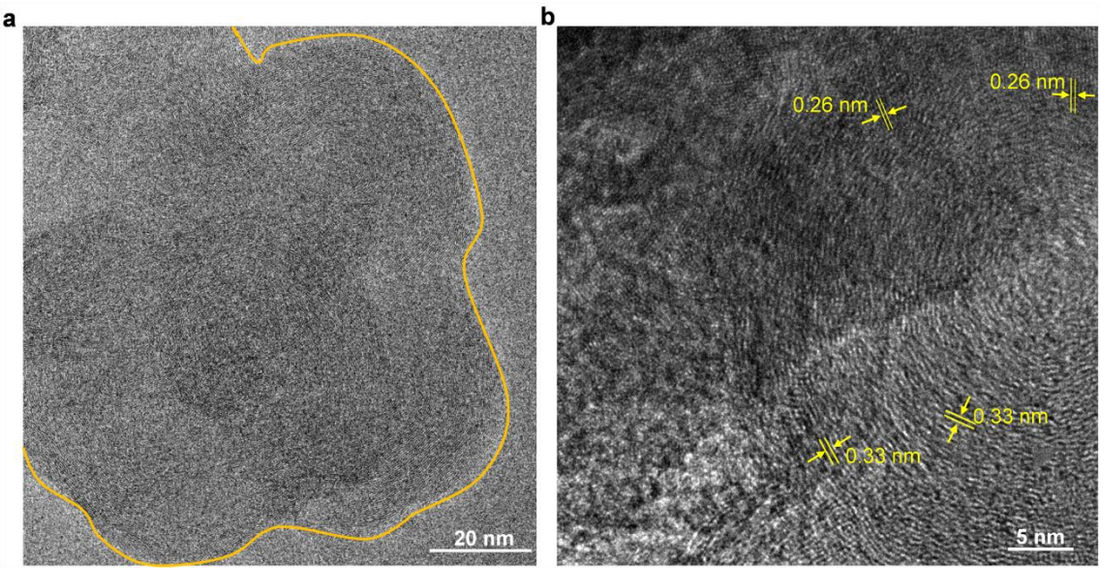

Fig. S23 (a-b) HRTEM images of t-MnO@C electrodes in the C-MOF-5@Zn||t-MnO@C cells detected at the fully discharge state in the first cycle, and the region surrounded the yellow lines suggest the insertion of Zn^{2+} in the electrode.

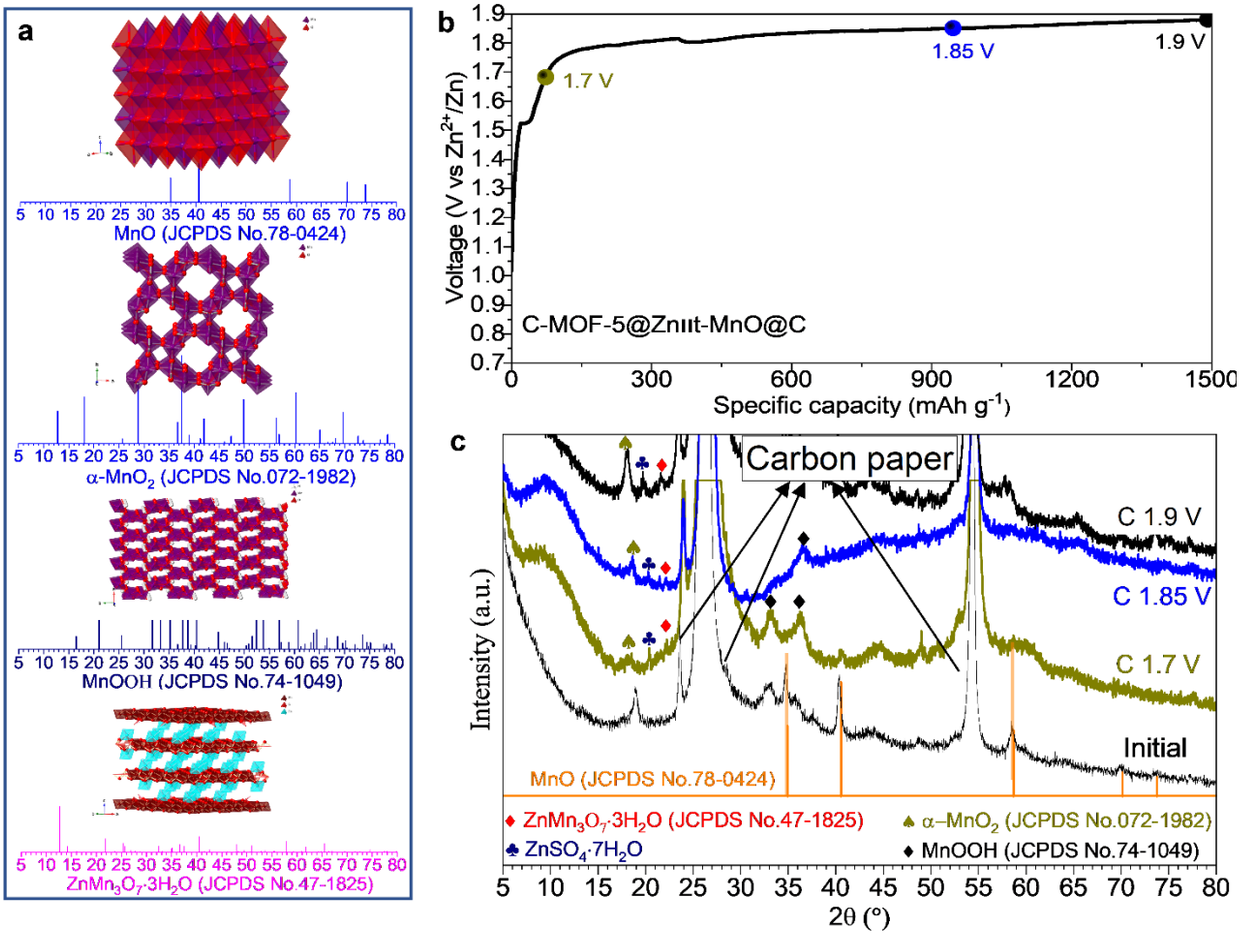

Fig. S24 (a) The simulated XRD patterns and crystal structure of products such as MnO, α-MnO_2, $ZnMn_3O_7 \cdot 3H_2O$ and MnOOH produced during the charging process in the first cycle at a current density of 0.05 A g^{-1} (b). (c) Ex-situ XRD patterns of the t-MnO@C electrode obtained in the C-MOF-5@Zn||t-MnO@C cell at different charge states during the charging process in the first cycle. In Fig. S24(c), "C" represents the charge state.

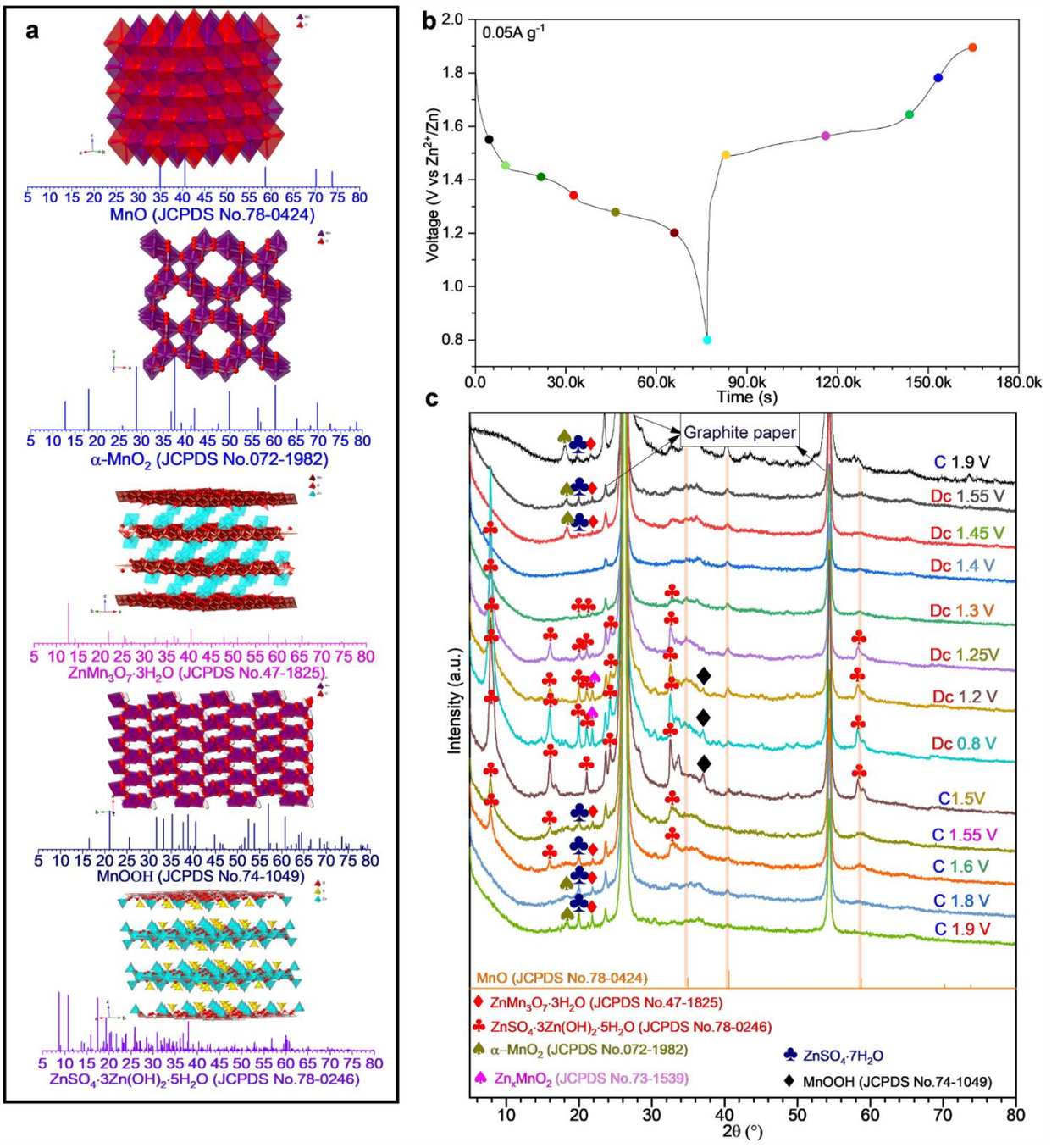

Fig. S25 (a) The simulated XRD patterns and crystal structure of products such as MnO, α-MnO_2, $ZnMn_3O_7 \cdot 3H_2O$, MnOOH and $ZnSO_4 \cdot 3Zn(OH)_2 \cdot 5H_2O$ produced during the discharging process in the first cycle and the charging process in the second cycle at a current density of 0.05 A g^{-1} (b). (c) Ex-situ X-ray diffraction patterns of the t-MnO@C electrode in the C-MOF-5@Zn||t-MnO@C cell at different states during the discharging process in the first cycle and charge states during the charging process in the second cycle. In Fig. S25(c), "C" represents the charge state; "Dc" represents the discharge state.

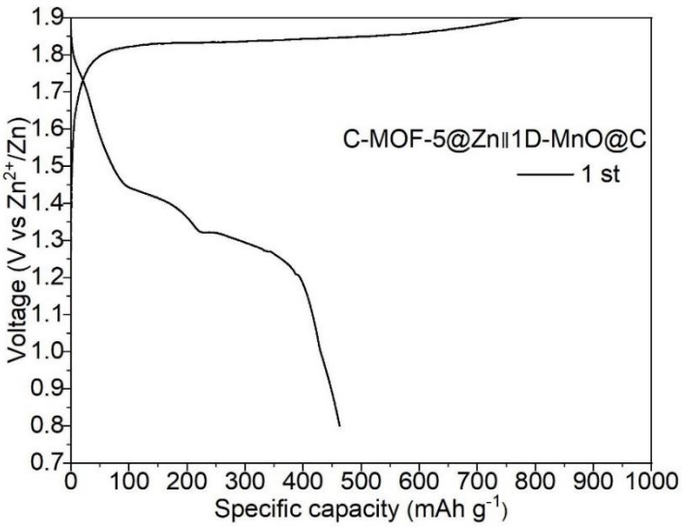

Fig. S26 Galvanostatic charge/discharge profiles of the 1D-MnO@C electrode in the C-MOF-5@Zn‖1D-MnO@C cell at a current density of 0.05 A g^{-1}. The discharge capacity in the first cycle is calculated to be 303 mAh g^{-1} after deducting the discharge capacity contribution of 159 mAh g^{-1} from the graphite paper current collector (see Fig. S20a).

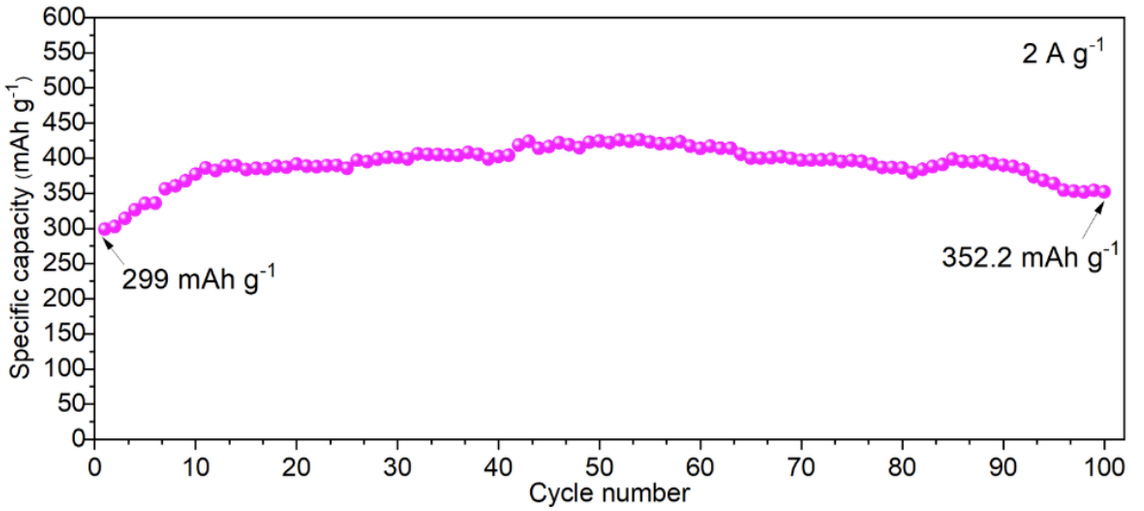

Fig. S27 The cycling performance of the t-MnO@C cathode in the C-MOF-5@Zn‖t-MnO@C cell at a current density of 2.0 A g^{-1}.

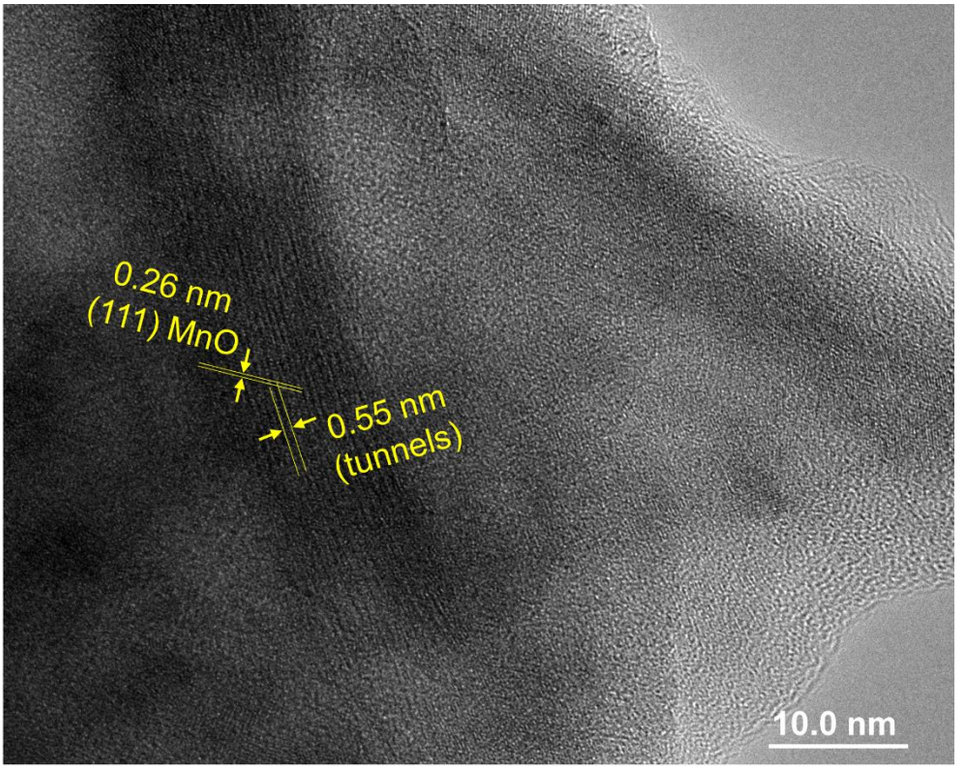

Fig. S28 HRTEM image of the t-MnO@C cathode material at the fully discharged state at 5 A g^{-1} after 20,000 cycles, showing the tunnels with a size of 0.55 nm.

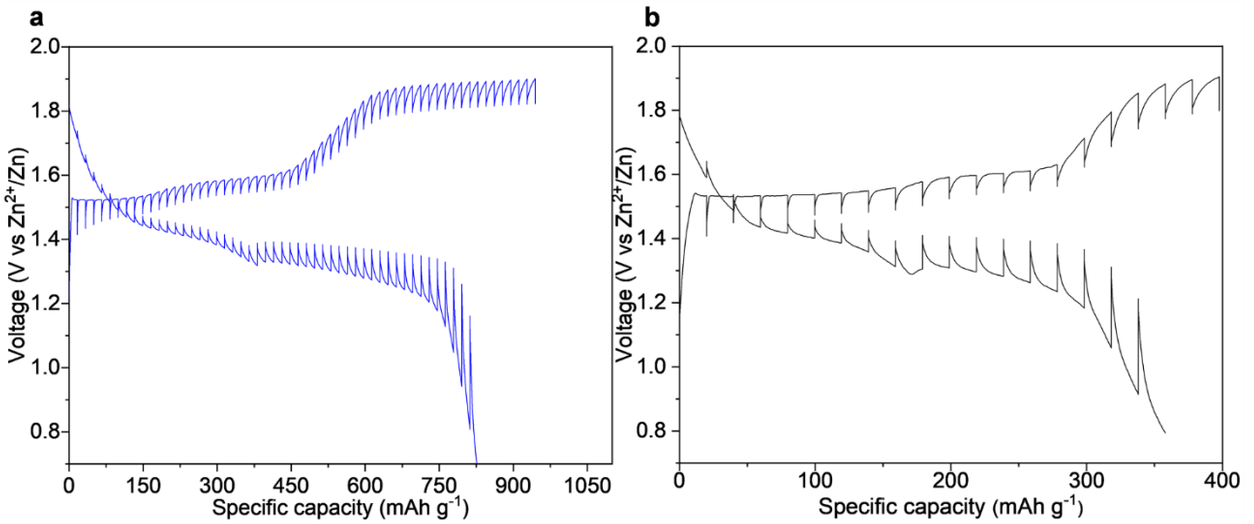

Fig. S29 The discharge/charge curves in the GITT measurement for (a) the t-MnO@C electrode in C-MOF-5@Zn||t-MnO@C and (b) the 1D-MnO@C electrode in C-MOF-5@Zn||1D-MnO@C cell.

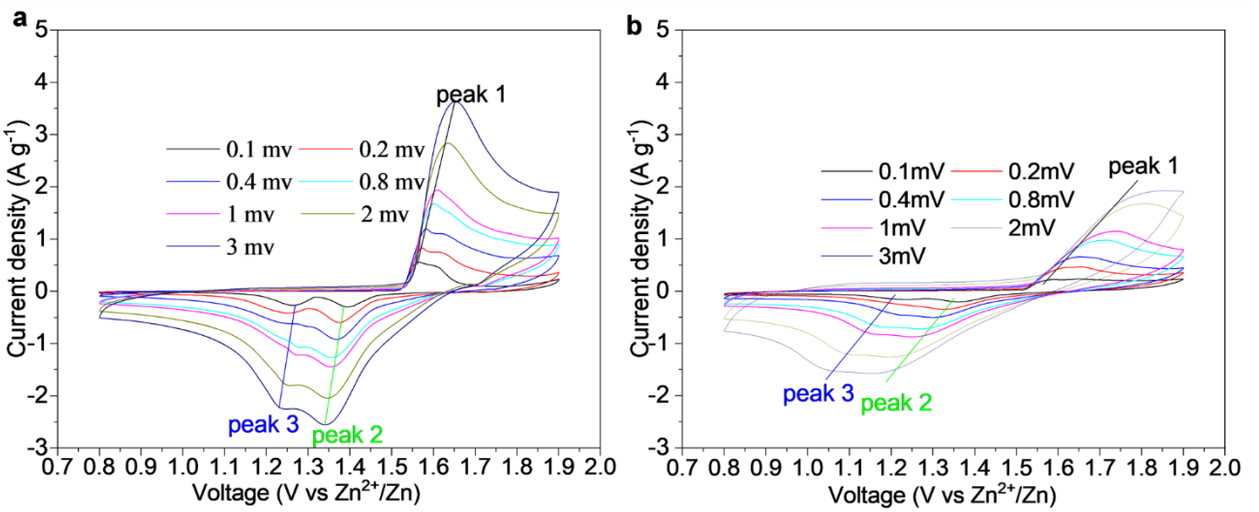

Fig. S30 CV profiles of (a) the t-MnO@C electrode in the C-MOF-5@Zn||t-MnO@C cell and (b) the 1D-MnO@C electrode in the C-MOF-5@Zn||1D-MnO@C cell measured at the second scan with the different scanning rate.

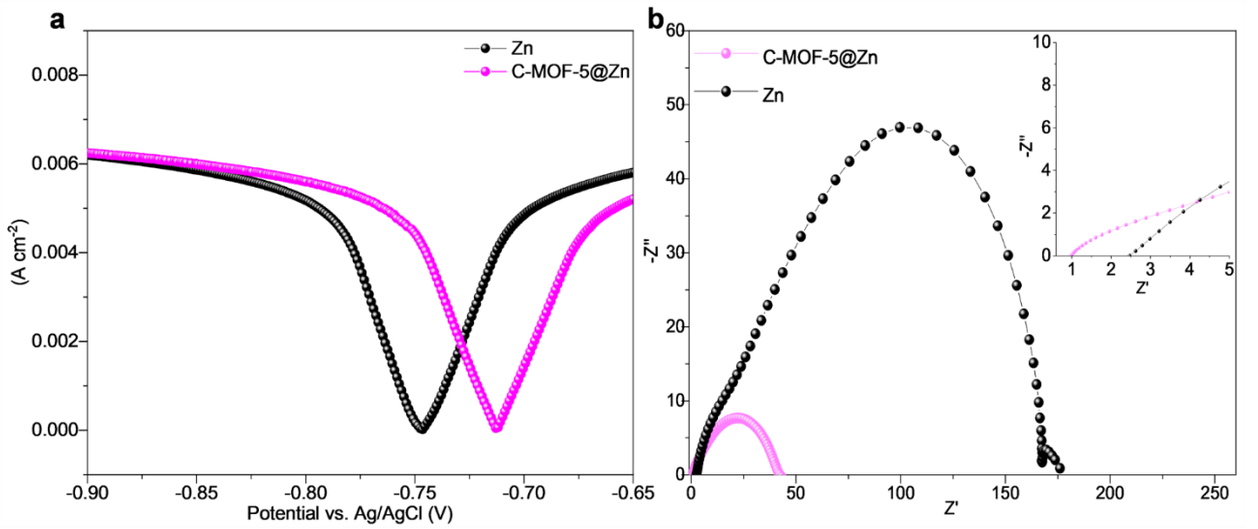

Fig. S31 (a) Liner polarization curves showing the corrosion on the bare Zn foil and C-MOF-5@Zn electrodes. (b) Electrochemical impedance spectra (EIS) of the C-MOF-5@Zn‖C-MOF-5@Zn and Zn‖Zn cells.

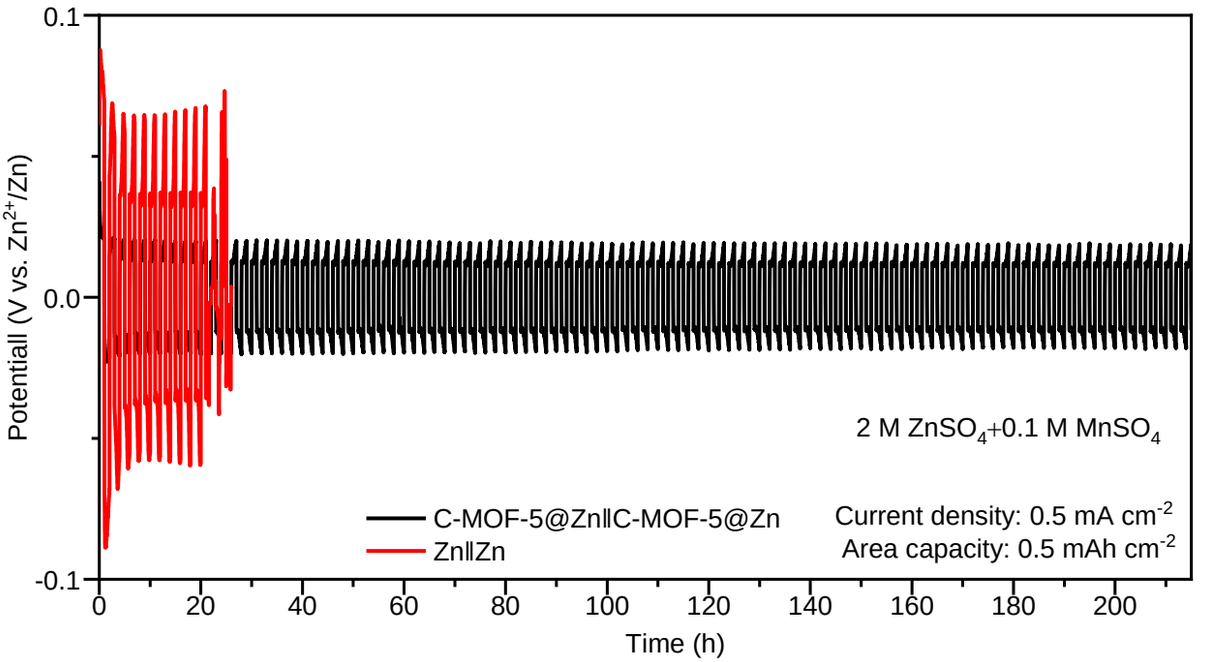

Fig. S32 (a) The Zn plating/striping process in the C-MOF-5@Zn‖C-MOF-5@Zn and Zn‖Zn symmetrical cells at high current density of 0.5 mA cm^{-2} with an areal capacity of 0.5 mAh cm^{-2}.

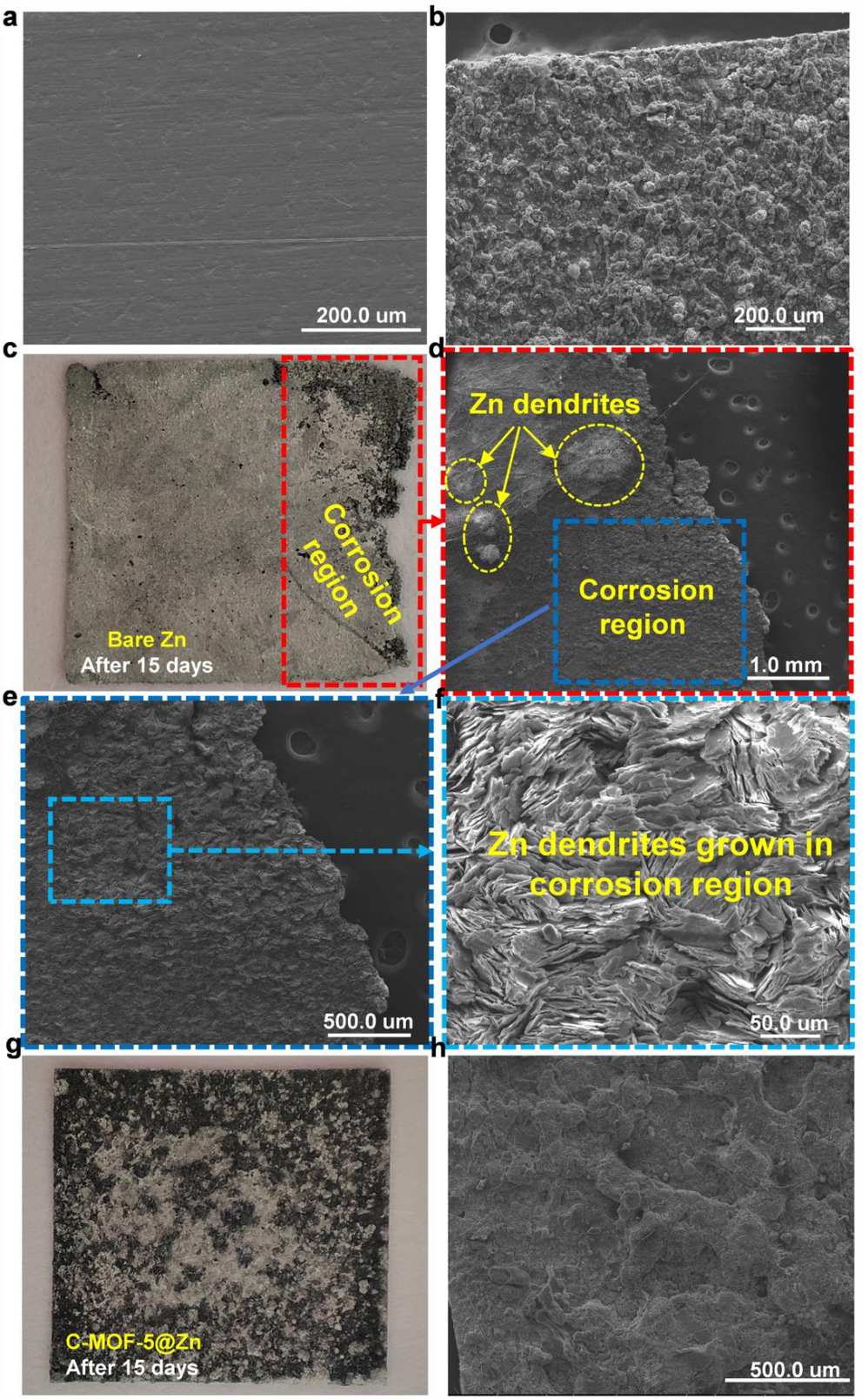

Fig. S33 SEM images of (a) the bare Zn anode and (b) C-MOF-5@Zn electrodes before cycling; optical photograph and SEM images of (e-f) the bare Zn and (g,h) C-MOF-5@Zn electrodes after cycling for 15 days.

Table. S1 Crystal data, data collection, and structure refinement parameters for 1D-MOF.

Name	**1D-MOF**
Chemical composition of MOF	$C_{30}H_{34}Mn_3N_4O_{16}$
Formula mass	871.43
Crystal system	monoclinic
Space group	*P* 2_1/c
a, Å	17.9106(3)
b, Å	11.79470(10)
c, Å	18.8396(3)
V, Å^3	3564.41(10)
Z	4
Measured reflections	6721
θ_{min} , º	2.755
θ_{max} , º	72.943
h	-21 to 22
k	-14 to 10
l	-22 to 22
Crystal size, mm^3	0.004*0.2*0.004
Temperature, K	150
CCDC number	2143646

Table. S2 Crystal data, data collection, and structure refinement parameters for L-MOF-HT.

Name	**L-MOF-HT**
Chemical composition of MOF	$C_7H_9MnNO_5$
Formula mass	242.09
Crystal system	trigonal
Space group	*P-3*
a, Å	14.1886(2)
b, Å	14.1886(2)
c, Å	8.1307(2)
V, Å^3	1417.55(5)
Z	6
Measured reflections	1880
θ_{min} , º	3.5560
θ_{max} , º	73.1330
h	-17 to 10
k	-15 to 17
l	-4 to 9
Crystal size, mm^3	1*0.3*0.3
Temperature, K	150
CCDC number	2143647

Table. S3 Comparisons of the electrochemical performance of this work with that of other Mn-based cathode materials.

Cathode materials	Initial discharge capacity /current density	Capacity retention/ cycles/current density	
MnO@NGS	288 mAh g^{-1} at 0.1 A g^{-1}	98%/300/0.5 A g^{-1}	R1
MnO@C	251 mAh g^{-1} at 0.1 A g^{-1}	70%/10000/2 A g^{-1}	R2
$Mn_{0.61}\square_{0.39}O$	300 mAh g^{-1} at 0.1 A g^{-1}	99.3%/1500/1 A g^{-1}	R3
δ-MnO_2	278 mAh g^{-1} at 0.308 A g^{-1}	98%/10000/6.16 A g^{-1}	R4
σ-MnO_2	345 mAh g^{-1} at 0.2 A g^{-1}	84%/2000/5 A g^{-1}	R5
α-MnO_2	285 mAh g^{-1} at 0.103 A g^{-1}	92%/5000/1.54 A g^{-1}	R6
β-MnO_2	258 mAh g^{-1} at 0.2 A g^{-1}	94%/2000/2 A g^{-1}	R7
γ-MnO_2-graphene	301 mAh g^{-1} at 0.5 A g^{-1}	64.1%/300/10 A g^{-1}	R8
δ-MnO_2	327 mAh g^{-1} at 0.2 A g^{-1}	76.8%/1000/1 A g^{-1}	R9
α-MnO_2	382.2 mAh g^{-1} at 0.3 A g^{-1}	94%/3000/3 A g^{-1}	R10
β-MnO_2	285 mAh g^{-1} at 0.0312 A g^{-1}	83.2%/1000/1.248 A g^{-1}	R11
$Na_{0.55}Mn_2O_4 \cdot 1.5H_2O$	288 mAh g^{-1} at 0.3 A g^{-1}	91%/1000/3 A g^{-1}	R12
t-MnO/t-MnO@C	743 mAh g^{-1} at 0.05 A g^{-1}	97%/20000/5 A g^{-1}	This work

References

[R1] W. Li, X. Gao, Z. Chen, R. Guo, G. Zou, H. Hou, W. Deng, X. Ji and J. Zhao, Chem. Eng. J., 2020, **402**. 125509.

[R2] S. Li, D. Yu, L. Liu, S. Yao, X. Wang, X. Jin, D. Zhang and F. Du, Chem. Eng. J., 2022, **430**. 132673.

[R3] C. Zhu, G. Fang, S. Liang, Z. Chen, Z. Wang, J. Ma, H. Wang, B. Tang, X. Zheng and J. Zhou, Energy Stor. Mater., 2020, **24**, 394-401.

[R4] D. Wang, L. Wang, G. Liang, H. Li, Z. Liu, Z. Tang, J. Liang and C. Zhi, ACS Nano, 2019, **13**, 10643-10652.

[R5] T. Xiong, Z. G. Yu, H. Wu, Y. Du, Q. Xie, J. Chen, Y. W. Zhang, S. J. Pennycook, W. S. V. Lee and J. Xue, Adv. Energy Mater., 2019, **9**. 1803815.

[R6] H. Pan, Y. Shao, P. Yan, Y. Cheng, K. S. Han, Z. Nie, C. Wang, J. Yang, X. Li, P. Bhattacharya, K. T. Mueller and J. Liu, Nat. Energy, 2016, **1**. 16039.

[R7] N. Zhang, F. Cheng, J. Liu, L. Wang, X. Long, X. Liu, F. Li and J. Chen, Nat Commun, 2017, **8**, 405.

[R8] C. Wang, Y. Zeng, X. Xiao, S. Wu, G. Zhong, K. Xu, Z. Wei, W. Su and X. Lu, J. Energy Chem., 2020, **43**, 182-187.

[R9] Z. Wang, K. Han, Q. Wan, Y. Fang, X. Qu and P. Li, ACS Appl. Mater. Interfaces, 2023, **15**, 859-869.

[R10] B. Wu, G. Zhang, M. Yan, T. Xiong, P. He, L. He, X. Xu and L. Mai, Small, 2018, **14**, e1703850.

[R11] M. Liu, Q. Zhao, H. Liu, J. Yang, X. Chen, L. Yang, Y. Cui, W. Huang, W. Zhao, A. Song, Y. Wang, S. Ding, Y. Song, G. Qian, H. Chen and F. Pan, Nano Energy, 2019, **64**. 103942.

[R12] Liu, Y. C. Wu, L. Huang, K. Liu, B. Duployer, P. Rozier, P. L. Taberna and P. Simon, Adv. Energy Mater., 2021, **11**. 2101287.